RSC Advances

PAPER

View Article Online
View Journal | View Issue



Cite this: *RSC Adv.*, 2026, **16**, 9155

# Synthesis of composite ZnO rods@mixed metal oxides derived from Zn–Fe-LDHs for the photocatalytic degradation of methylene blue

Nguyen Thi Mai Tho, *[a] Minh An Tran Nguyen, [a] Huynh Tu Khanh,[a] T. V. M. Sreekanth [b] and Nguyen Thi Hong Anh[c]

ZnO rods/mixed metal oxides, derived from a layered double hydroxide (ZO@ZFO), were effectively synthesised using a simple and efficient coprecipitation method. XRD, FT-IR, SEM, XPS, DRS and EDX were used to investigate the synthesised materials. ZFO consists of two phases, ZnO and $ZnFe_2O_4$, uniformly distributed on ZnO rods. The photocatalytic efficacy of ZO@ZFO was assessed by decomposing methylene blue (MB) under visible-light conditions. The ZO@ZFO heterojunction, with a ZnO/ZFO mass ratio of 10%, achieved a MB removal efficiency of 95.8%, markedly surpassing those of ZO (54.73%) and ZFO (77.48%) under identical conditions: a catalyst loading of 1.0 g $L^{-1}$, 40 ppm of MB concentration, pH of 8, and 150 minutes of halogen lamp irradiation. The first-order kinetic simulation for the photocatalytic process yielded optimal results with $k_1$ = 0.01854 $min^{-1}$ and $r_1^2$ = 0.94314–0.9977. The effectiveness of photodegradation was evaluated under various conditions, including catalyst loading, initial MB concentration, and pH. The traditional type II mechanism for degrading MB *via* the ZO@ZFO heterojunction was presented. These findings underscore the significant potential of LDH-derived mixed-oxide heterojunctions for photocatalysis.

Received 14th December 2025
Accepted 27th January 2026

DOI: 10.1039/d5ra09661h

rsc.li/rsc-advances



## 1. Introduction

The textile industry ranks as the second-largest industry globally, releasing the majority of its effluent, which contains dyes, either untreated or inadequately treated.[1,2] Consequently, removing harmful dyes from textile effluent to maintain an environmentally sustainable condition is a significant problem.[3] Photocatalysis is a promising method within advanced oxidation processes (AOPs) for the remediation of persistent organic pollutants.[3–5] The photocatalytic process utilises diverse semiconductor materials that absorb light to produce electron–hole pairs and reactive oxygen species ($^{\bullet}OH$ and $^{\bullet}O_2^-$), which subsequently break down organic contaminants.[2,6,7] Consequently, it is imperative to synthesise semiconductor materials that fulfil criteria including cost-effectiveness, ease of synthesis, efficient decomposition of pollutant chemicals, and enduring photocatalytic stability.[8,9]

Recently, mixed metal oxides (MMOs) derived from LDHs have attracted wide attention as potential photocatalysts due to their large specific surface area and facile synthesis methods.[10] LDH, a type of anionic clay characterised by a two-dimensional layered structure, has the general formula $[M^{2+}_{1-a}M^{3+}_{a}(OH)_2]^{a+}\cdot[A^{n-}_{a/n}]\cdot mH_2O$, where $M^{2+}$, $M^{3+}$, and $A^{n-}$ indicate divalent metal ions, trivalent metal ions, and anions, respectively. The hydroxide layer $[M^{2+}_{1-a}M^{3+}_{a}(OH)_2]^{a+}$ has a positive charge, whereas the interlayer $[A^{n-}_{x/n}]\cdot mH_2O$ represents anions that neutralise the positive charge of the hydroxide layers. The change in ionic composition with varying molar ratios enables LDH to adjust its structure adeptly.[6,11] A distinctive characteristic of LDH is that calcination at moderate temperatures (300–600 °C) results in the formation of highly active, non-stoichiometric mixed metal oxides with substantial specific surface areas, which can enhance photocatalytic activity by generating numerous active sites.[12–14] Based on the aforementioned facts, MMOs have demonstrated significant potential across various applications, particularly in photocatalysis. However, MMOs have some limitations, such as rapid electron–hole recombination and low quantum efficiency under light.[6] To address this issue, various improvement methods have been implemented, including doping and combination with different semiconductor materials.[8,10,15,16] Feipeng Jiao compared the photocatalytic performance of three materials, namely, ZnCo-LDH, MMO derived from LDH (ZnCo-cLDH), and combined BiOI/ZnCo-cLDH composites with BiOI/ZnCo-cLDH mass ratios of 1, 3, 5, 7, and 10%, respectively, to treat tetracycline hydrochloride (TCH). Under the same photocatalytic conditions, the results indicated that ZnCo-cLDH had a TCH

[a]*Faculty of Chemical Engineering, Industrial University of Ho Chi Minh City, Ho Chi Minh, Vietnam. E-mail: nguyenthimaitho@iuh.edu.vn*

[b]*School of Mechanical Engineering, Yeungnam University, Gyeongsansi, Gyeongsangbukdo, Republic of Korea*

[c]*Faculty of Chemical Engineering, Ho Chi Minh City University of Industry and Trade, 140 Le Trong Tan Street, Tay Thanh Ward, Tan Phu District, Ho Chi Minh, Vietnam*

decomposition efficiency of 45.9%, which was higher than that of ZnCo-LDH (41.29%). The hybrid photocatalyst BiOI/ZnCo-cLDH, with a mass ratio of 5% (BiOI/cLDH-3), exhibited the best TCH decomposition efficiency (86.6%).[17] Furthermore, several investigations have effectively synthesised hybrid materials using cLDHs, including Cu-doped ZnO/calcined CoFe-LDH composites,[6] Cnt@calcined Zn–Co-LDH,[18] and $gC_3N_4$/MgZnAl MMOs derived from LDH.[19]

Zinc oxide (ZnO) is a semiconductor that exists in many different forms, including nanostrips, nanosheets, nanodots, nanotubes, nanorods, and microspheres.[20–22] ZnO rods with a one-dimensional (1D) structure have been extensively studied in the field of photocatalysis.[21] ZnO has a large band gap energy (3.1–3.37 eV), which restricts its absorption to the UV region exclusively.[20,21] Consequently, multiple methods have been employed to enhance the visible-light absorption capacity of ZnO. This study proposes the synthesis of ZO/ZFO derived from ZnFe-LDH composite rods as photocatalytic materials for treating textile wastewater. Initially, ZnO rods are synthesised, followed by the dispersion of CoFe-LDH on the surface of ZnO rods using the coprecipitation method. ZnO rods/MMOs were formed from ZnO rods/ZnFe-LDH by calcination.

# 2. Experimental

## 2.1 Synthesis of ZnO rods

$Zn(NO_3)_2$ 0.5 M solution (100 mL) was introduced at a flow rate of 2 mL $min^{-1}$ into a beaker containing 100 mL of NaOH 0.5 M solution, which is located in an ultrasonic bath. The reaction yielded a white precipitate and maintained a pH value of 11 throughout the process. Upon completion of the reaction, ultrasonication of the white precipitate was sustained for an extra 2 hours to stabilise the structure. The precipitate was then filtered and rinsed with distilled water until the wash water reached pH 7.[23] The sample was dried at 105 °C and then heated to 500 °C for 4 hours; the resultant white product was labelled ZO.

## 2.2 Synthesis of ZnO rods@mixed metal oxide derived from Zn–Fe-LDH

ZnO (m (g)) was evenly dispersed in 100 mL of NaOH 0.5 M solution, referred to as mixture A. Solution B comprised 50 mL of $Zn(NO_3)_2$ 0.3 M and 50 mL of $Fe(NO_3)_3$ 0.1 M, yielding a molar ratio of $Zn^{2+}/Fe^{3+} = 3/1$. Solution B was slowly added to solution A at a rate of 2 mL $min^{-1}$, and the pH was stabilised to 10 with NaOH solution, with constant stirring during the reaction. The resultant suspension was transferred to a 500 mL flask, thereafter agitated, and refluxed for 2 hours at 100 °C. The resultant precipitate was subjected to centrifugation, repeatedly rinsed with deionised water, and thereafter dried at 100 °C for 4 hours. The yellow item was heated to 600 °C for 4 hours. The mass ratios of ZO/ZFO were 0%, 5%, 10%, and 15%, with the samples designated as ZFO, 5ZO@ZFO, 10ZO@ZFO, and 15ZO@ZFO, respectively. Especially with sample ZFO, the synthesis procedure was similar to that of ZO@ZFO; nevertheless, solution A lacked ZO.

The synthesised ZO, ZFO, and ZO@ZFO samples were characterised using X-ray diffraction (XRD), Fourier-transform infrared spectroscopy (FT-IR), transmission electron microscopy (TEM), scanning electron microscopy (SEM), X-ray photoelectron spectroscopy (XPS), UV-visible diffuse reflectance spectroscopy (DRS), and energy-dispersive X-ray spectroscopy (EDX).

## 2.3 Preparation of the photocatalysts

The photocatalytic efficiency of the as-synthesised materials was evaluated by studies on MB dye degradation under visible light. This study employed visible-light simulation using a halogen lamp (Osram, Germany, model 64640 HLX 150 W, 24 V) without a filter to direct irradiate the catalytic system. The catalyst system has two glass layers; the inner layer contains 0.1 g of ZO@ZFO uniformly distributed in 100 mL of MB at an initial concentration of 40 ppm, while the outer layer circulates water to maintain temperature stability throughout the photocatalytic process. The catalytic process has two phases: (i) light-off, which enables the catalytic material to attain adsorption–desorption equilibrium within 60 minutes. Subsequently, 3 mL of the appropriate solution was filtered through a 0.22 μm filter to remove particles, and the MB content was assessed. (ii) Light on: The apparatus was lit for 150 minutes to execute the photocatalytic process. At 30 minutes intervals, 3 mL of the suspension was extracted, and the MB concentration was quantified. MB concentration is measured using a UV-vis spectrophotometer at 665 nm.

Factors affecting the photocatalytic activity of ZO@ZFO were also investigated, including the ZO/ZFO mass ratio, catalyst loading, initial MB concentration, and pH.

# 3. Results and discussion

## 3.1 Phase composition and morphology

The crystal structures of the ZO, ZFO, 5ZO@ZFO, 10ZO@ZFO, and 15ZO@ZFO samples were elucidated using X-ray diffraction (Fig. 1A). The ZO sample exhibited peaks at $2\theta$ values of 31.4° (100), 34.4° (002), 36.2° (101), 47.6° (102), 56.6° (110), 62.7° (200), 67.93° (112) and 69.1° (004), which are indicative of ZnO (JCPDS no. 36-145).[24] ZFO had diffraction peaks at the positions of 29.9°, 35.3°, 42.8°, 53.2° and 62.24°, corresponding to the planes of (220), (311), (400), (422) and (440), respectively, of spinel $ZnFe_2O_4$ (JCPDS card no. 22-1012).[25] In addition, the principal peaks indicative of the ZnO phase were present, but with lower intensity than pure ZnO. The findings indicated that ZFO has two phases, $ZnFe_2O_4$ and ZnO, consistent with prior research on these composites. The ZFO sample was synthesised with a molar ratio of $Zn^{2+}/Fe^{3+} = 3/1$, characteristic of LDH. Following calcination at 600 °C, the LDH disintegrated, resulting in the formation of the corresponding MMOs: $ZnFe_2O_4$ and ZnO. Fig. 1B shows that the diffraction peaks at $2\theta$ angles of 31.4° (100), 33.1° (002), and 36.8° (101) in the ZFO sample, associated with ZnO, exhibit a minor shift relative to pure ZnO. This alteration is attributable to the interaction between $ZnFe_2O_4$ and ZnO during LDH calcination, resulting in

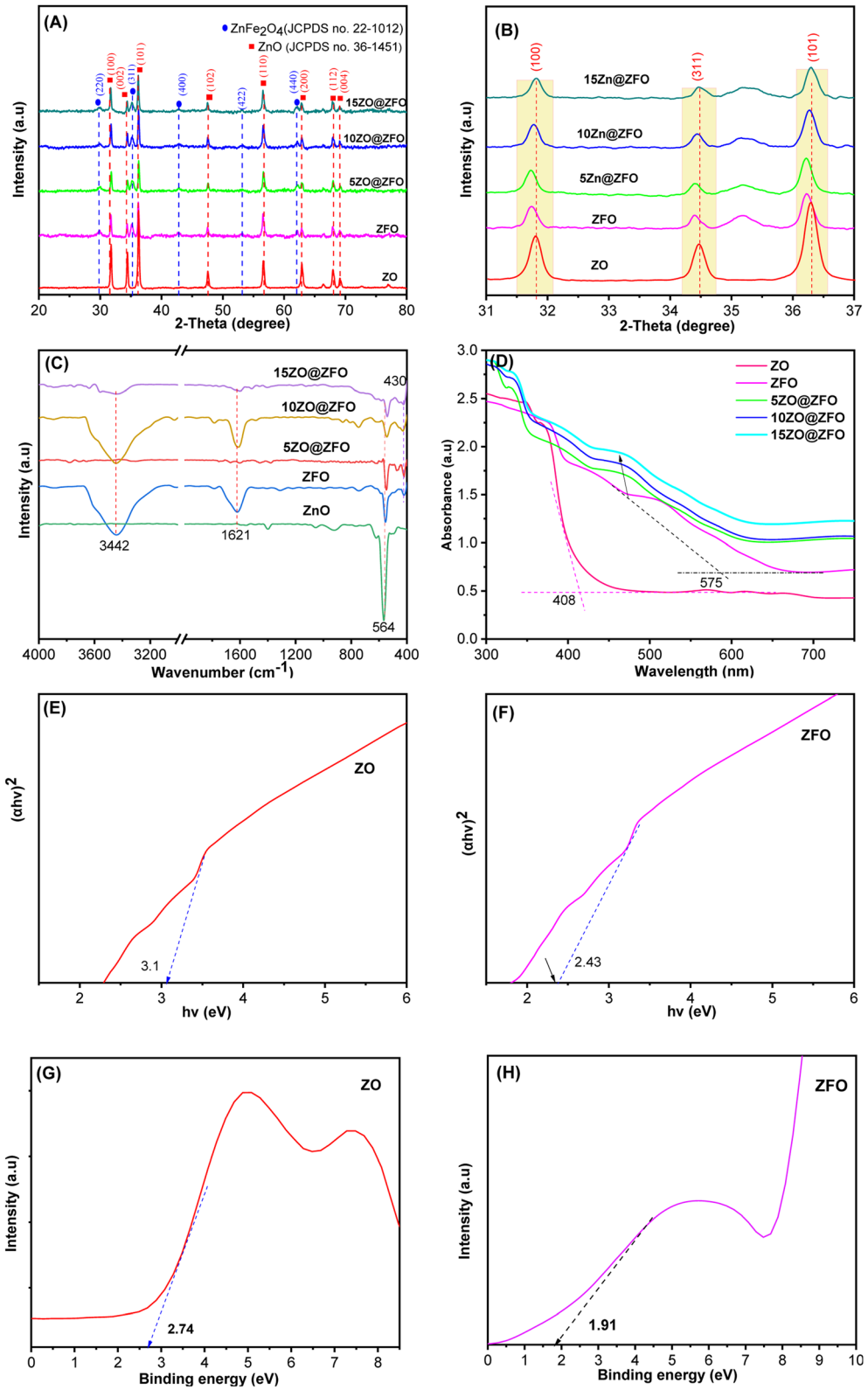


Fig. 1 (A) and (B) XRD patterns; (C) FT-IR spectra and (D) UV-vis DRS spectra of ZO, ZFO, and ZO@ZFO samples. (E) and (F) Energy band gaps of ZO and ZFO determined using the Tauc equation and (G) and (H) valence band XPS spectra of ZO and ZFO.

properties distinct from those of pure ZnO. ZFO precipitates on the surface of ZO, with mass ratios of ZO/ZFO at 5%, 10%, and 15%, respectively. The XRD results for these samples indicated that, in addition to the typical peaks of the two phases, $ZnFe_2O_4$ and ZnO, no anomalous peaks were observed, confirming the high purity and minimal contamination of the composites.

Furthermore, Fig. 1B illustrates a pronounced red shift of the characteristic peaks of ZnO in the ZO@ZFO sample relative to pure ZnO.

The FT-IR spectra of the synthesised samples are shown in Fig. 1C. The observable absorption bands at around 1600 $cm^{-1}$ and 3300–3500 $cm^{-1}$ correspond to the bending and stretching vibrations of water, respectively. The ZO sample has an absorption peak at 564 $cm^{-1}$, corresponding to the stretching vibration of the Zn–O bond. The ZFO sample exhibits absorption at 564 $cm^{-1}$ and 430 $cm^{-1}$, corresponding to the vibrations of Zn–O and Fe–O, respectively.[26] The 5ZO@ZFO and 10ZO@ZFO samples exhibit absorption peaks similar to those of ZFO; however, the peak intensities increase with increasing ZnO concentration in the ZO@ZFO samples. The XRD and FTIR data indicate a chemical interaction between the phases in ZO@ZFO.

The UV-vis DRS spectra assess the capacity to absorb photons and facilitate electron transport from a low-energy state to a high-energy state while providing comprehensive insights into the energy band gap ($E_g$) in semiconductor materials. Fig. 1D illustrates the UV-vis DRS findings of the synthesised samples. ZO has a pronounced absorption edge at 408 nm within the UV spectrum, a characteristic feature of ZnO. ZFO has an absorption edge at 575 nm within the visible spectrum. A previous study indicated that pure $ZnFe_2O_4$ exhibited significant absorption in the 650–700 nm region.[27] The XRD results shown in Fig. 1A demonstrate that ZFO comprises two phases, ZnO and $ZnFe_2O_4$, which are produced after the thermal treatment of Zn–Fe-LDH. Therefore, the interaction between these two phases changes the absorption spectrum of the ZFO sample compared with pure ZnO and pure $ZnFe_2O_4$.[10,15] The combination of ZFO and ZO in varying ratios results in a blue shift in the absorption wavelength relative to ZFO and a red shift relative to ZO; the shift intensity increases with increasing ZnO loading. The deposition of ZFO nanoparticles on ZnO enhances the composite's visible-light absorption, improving the ZO@ZFO heterojunction's photocatalytic effectiveness.[28] The $E_g$ is calculated using the Tauc equation from the material's maximum absorption wavelength. As shown in Fig. 1E and F, the $E_g$ of ZO and ZFO was 3.1 eV and 2.43 eV, respectively. Fig. 1G and H displays the XPS valence band spectra of ZnO and ZFO. By establishing the cut-off point between the leading edges of the linearly extrapolated background valence band, the valence band maximum (VBM) location was determined.[29,30] The VBM values for ZnO and ZFO were 3.2, 2.2, and 0.2 eV, respectively.

The SEM images of the samples are shown in Fig. 2A–D. The SEM images were obtained at a magnification of ×60.0k and a scale of 500 nm, revealing that the ZFO l surface is spherical and exhibits a porous, entirely heterogeneous nanostructure, with dimensions ranging from 20 to 60 nm. ZnO has a unique elongated rod shape with a rough surface, a diameter of about 80–150 nm, and a length of several hundred nanometers. The ZO@ZFO samples indicate that the ZFO particles are irregularly distributed across the ZnO surface, resulting in a dense contact network between the two phases. The extensive contact area enhances the separation and transfer efficiency of electrons and holes at the ZFO–ZnO interface. An increase in ZO content within the ZO@ZFO samples correlates with a decrease in ZFO coverage density. The TEM images of ZO@ZFO (Fig. 2E) vividly reveal the heterogeneous composite's unique morphological structure. A significant contrast between bright and dark areas is evident in the ZnO rods; the darker spots along the rods indicate the presence of ZFO nanoparticles. This confirms the successful formation of the ZO@ZFO heterogeneous structure, in which ZFO is directly bonded to the ZnO surface, thereby establishing a strong interfacial connection between the two components. EDX analysis of the 10ZO@ZFO sample (Fig. 2F) revealed the presence of O (17.15 wt%), Zn (58.11 wt%), and Fe (24.33 wt%), while EDX mapping verifies the homogeneous distribution of these elements.

XPS spectrum to determine the composition and oxidation state of elements on the surface of ZFO; 10ZO@ZFO samples were used.[31] Fig. 3 presents the XPS survey spectrum of ZFO and ZO@ZFO samples, together with the associated high-resolution spectra for Fe 2p, O 1s, and Zn 2p. The full-spectrum analysis of the ZFO and 10ZO@ZFO samples revealed the presence of Zn, Fe, and O, with no extraneous elements identified, indicating that the synthesized materials exhibit great purity and are free from impurities (Fig. 3A). The percentage contents of the Zn, Fe, and O elements in the two samples differ; concurrently, the high-resolution spectrum of Zn 2p, Fe 2p, and O 1s changes variations in binding energy, detailed as follows:

The high-resolution XPS spectra of Zn 2p (Fig. 3B), including two peaks at energy levels of 1021.4 eV and 1044.43 eV, attributed to Zn $2p_{3/2}$ and Zn $2p_{1/2}$, respectively, validated the existence of $Zn^{2+}$ in the ZFO. The binding energies of Zn $2p_{3/2}$ and Zn $2p_{1/2}$ in the 10ZnO@ZFO sample exhibited positive shifts of 0.67 eV and 0.84 eV, respectively, in comparison with the ZFO sample. The peaks in the Fe 2p spectrum (Fig. 3C) with binding energies of 710.48 eV and 724.36 eV correspond to the $2p_{3/2}$ and $2p_{1/2}$ states, respectively. The deconvolution of these two peaks indicates that the peaks at energy levels of 710.48 and 723.66 eV correspond to $Fe^{3+}$, whereas the peaks at 712.2 and 725.35 eV correspond to $Fe^{2+}$. Furthermore, the presence of iron ions in a multivalent state is indicated by two satellites at 720 eV and 733 eV within the ZFO.[32,33] The Fe 2p spectrum of 10ZO@ZFO displays peaks similar to those of ZFO, although with a positive shift relative to ZFO. The O 1s spectrum (Fig. 3D) shows two distinct peaks at 529.3 eV and 531.3 eV, respectively. The former peak represents the typical value of crystalline oxygen (M–O) on the composite material's surface, while the latter peak arises from defect sites in the spinels. Analysis of high-resolution XPS spectra revealed that the binding energies of Zn 2p, Fe 2p, and O 1s of ZO@ZFO vary from those of ZFO, signifying alterations in the electron cloud density around Zn, Fe, and O. This results from the redistribution of interface charges and the Fermi-level equilibrium between the ZO and ZFO phases, thereby diminishing the recombination of light-generated electrons and holes. This enhancement improves the photocatalytic degradation efficiency of ZO@ZFO.[33,34]

### 3.2 Photodegradation evaluation

**3.2.1 Effect of catalyst type.** The photocatalytic efficacy of the synthesised materials was assessed by measuring the

 

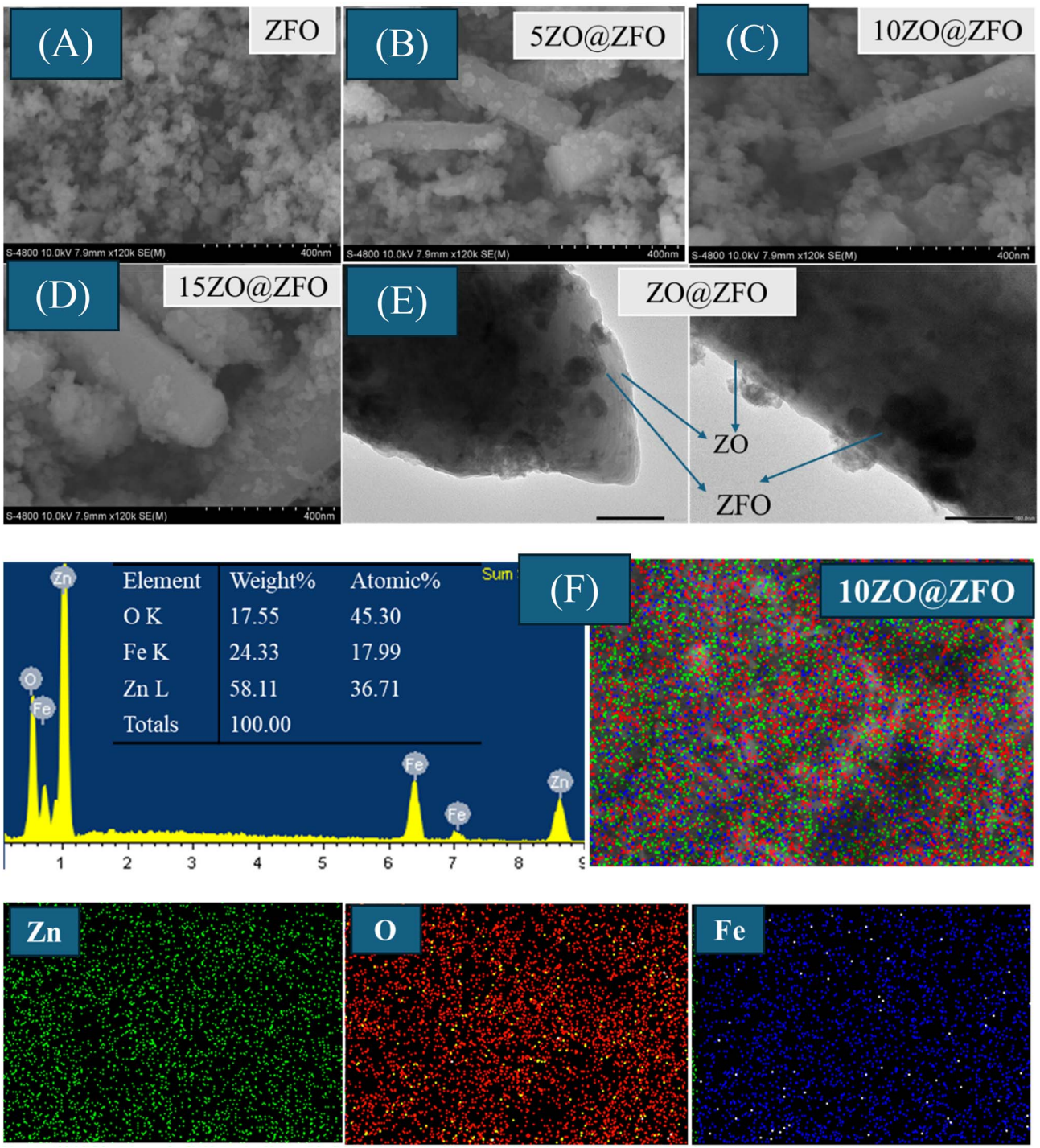


Fig. 2 SEM images of (A) ZFO, (B) 5ZO@ZFO, (C) 10ZO@ZFO, and (D) 15ZO@ZFO; (E) TEM images of ZO@ZFO; and (F) EDX elemental mapping images and EDS spectrum of 10ZO@ZFO.

degradation of MB under visible light using the following parameters: catalyst loading, 1.0 g $L^{-1}$; MB concentration, 40 ppm; adsorption duration, 60 minutes; and photocatalytic duration, 150 minutes (Fig. 4A and B). The experimental results indicated that, after 60 minutes of adsorption, the materials reached equilibrium and desorbed in around 45 minutes, processing a maximum of about 27% of MB. The photocatalytic activity changed significantly after 150 minutes of light exposure. The results indicated that ZO and ZFO processed just 48.94% and 79.5% of the MB, respectively. The UV-vis spectral analysis revealed that ZnO has a high band gap energy, absorbing only in the ultraviolet spectrum, whereas ZFO can absorb in the visible spectrum, leading to a comparatively higher efficiency. However, ZO and ZFO combined in different

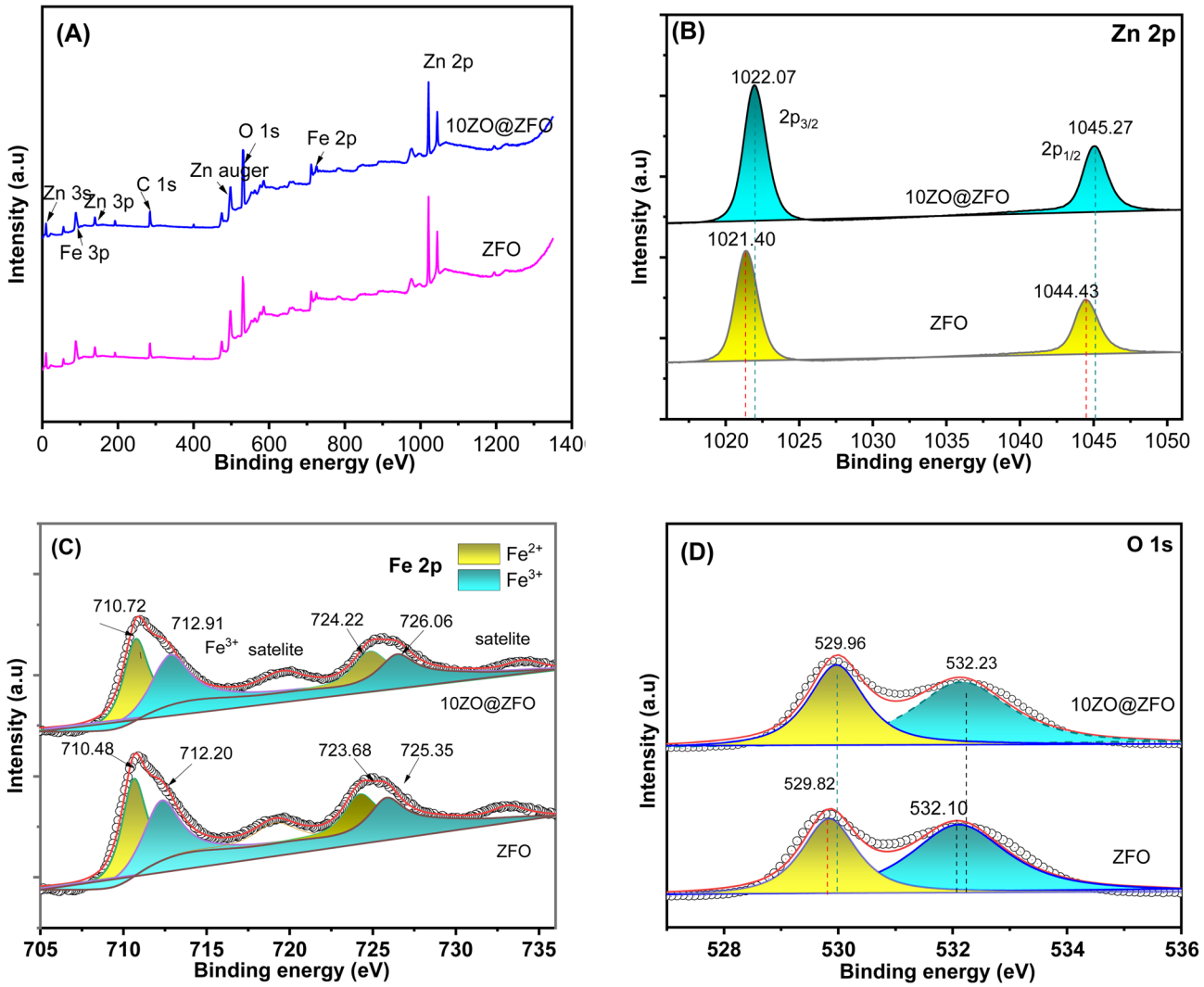


Fig. 3 XPS survey spectra of (A) ZFO and 10ZO@ZFO; high-resolution spectra of (B) Zn 2p, (C) Fe 2p, and (D) O 1s.

mass ratios showed a significant improvement in the photocatalytic efficiency of MB breakdown, increasing by 89.94%, 95.8%, and 92.74% for 5ZO@ZFO, 10ZO@ZFO, and 15ZO@ZFO, respectively. Furthermore, the surface area of ZO@ZFO also enhances its light absorption, thereby improving its efficacy in decomposing MB; therefore, optimising the ZFO/ZO ratio is crucial. If ZnO is extensive, it obstructs light from reaching the ZFO surface, diminishing the effectiveness of MB breakdown.[26,30] This investigation showed the MB-degrading efficacy of the synthesised photocatalyst under visible light, ranked as follows: ZO < ZFO < 5ZO@ZFO < 15ZO@ZFO < 10ZO@ZFO. The 10ZO@ZFO sample with a ZO/ZFO mass combination ratio of 10% was confirmed to be the most effective for MB degradation.

The XRD and XPS spectra demonstrate chemical interaction between ZO and ZFO, leading to the formation of interphase heterojunctions, establishing charge–exchange interfaces and increasing the production of reactive oxygen species (ROS), thereby improving MB degradation.[25,35] The surface area of ZO@ZFO also enhances its light absorption, thereby improving its efficacy in decomposing MB; therefore, optimising the ZFO-to-ZO ratio is crucial. If ZnO is extensive, it obstructs light from reaching the ZFO surface, diminishing the effectiveness of MB breakdown.[36,37] This investigation showed the MB-degrading efficacy of the synthesised photocatalyst under visible light, ranked as follows: ZO < ZFO < 5ZO@ZFO < 15ZO@ZFO < 10ZO@ZFO. The 10ZO@ZFO sample with a ZO/ZFO mass combination ratio of 10% was confirmed to be the most effective for MB degradation.

The change in MB concentration ($C_t$) over time ($t$) during photocatalysis was recorded. The pseudo-zero-, first-, and second-order kinetic equations for the MB degradation process of the synthesised materials are presented in Fig. 4, C, D, E and Table 1. In this context, $k_0$, $k_1$, and $k_2$ are the apparent kinetic rate constants for zero-, first-, and second-order reaction kinetics, respectively.[38] The correlation coefficient values ($r^2$) for the zero-, first-, and second-order kinetic equations are as follows: $r_0^2$ = 0.92808–0.94904; $r_1^2$ = 0.94314–0.9977; $r_2^2$ =

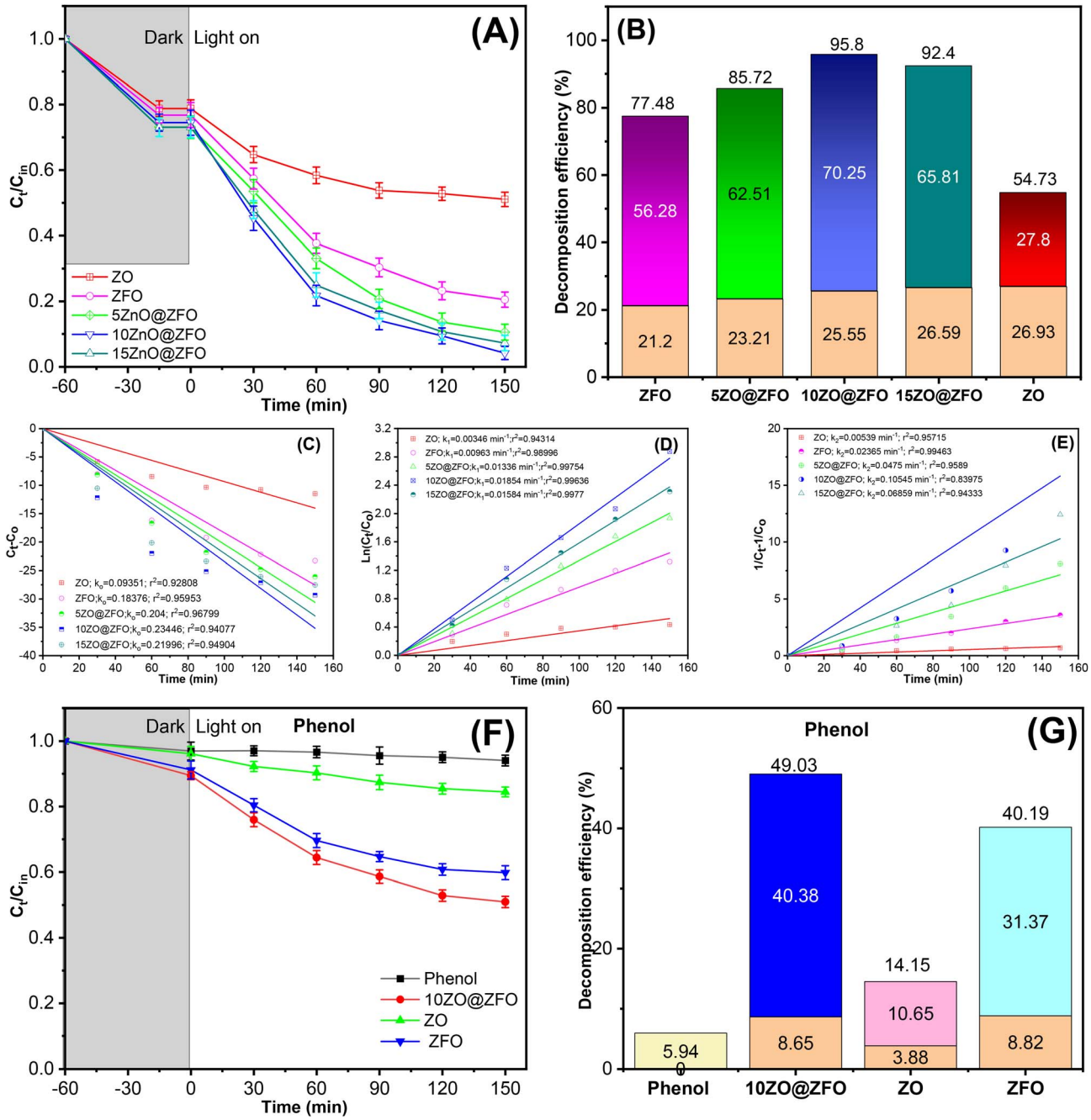


Fig. 4 (A) and (B) Photocatalytic efficiency of the synthesised materials in decomposing MB, (C) zero-order kinetics plots, (D) first-order kinetics plots, and (E) second-order kinetics plots. (F) and (G) Photocatalytic efficiencies of the synthesised materials in decomposing phenol.

0.83975–0.99463. These results indicate that the pseudo-first-order model is the most accurate representation of the photocatalytic process for MB compared with the zero- and second-order models. The MB degradation rate of 10ZO@ZFO reached 0.01854 $min^{-1}$, which was double that of pure ZFO ($k_1$ = 0.00963 $min^{-1}$).

MB is a visible-light-responsive dye that functions as a photosensitiser by absorbing photons; therefore, it is crucial to distinguish between dye-sensitised degradation and the intrinsic photocatalysis of ZO@ZFO. Phenol was proposed as a non-photosensitising probe molecule to address this problem. In contrast to MB, phenol does not absorb visible light and exhibits only an absorption edge in the UV region (~270 nm).[39] The photocatalytic degradation of phenol in ZO, ZFO, and 10ZO@ZFO under visible light was evaluated using a catalyst dosage of 1.0 g $L^{-1}$, an initial phenol concentration of 10 ppm, a dark adsorption period of 60 min, and an irradiation duration of 150 min (Fig. 4F and G). Phenol showed very little deterioration (~6%) under visible light in the absence of a catalyst, indicating that it does not directly photolyse or degrade *via* self-

Table 1 Correlation coefficient and rate constant values of the kinetic models for the degradation of MB in ZO, ZFO, and ZO@ZFO

| | Zero order | | First order | | Second order | |
|---|---|---|---|---|---|---|
| | $C_t - C_o = k_o t$ | | $\ln\left(\frac{C_o}{C_t}\right) = k_1 t$ | | $\frac{1}{C_t} - \frac{1}{C_o} = k_2 t$ | |
| Samples | $r_0^2$ | $k_o$ (mg $L^{-1}$ $min^{-1}$) | $r_1^2$ | $k_1$ ($min^{-1}$) | $r_2^2$ | $k_2$ (L $mg^{-1}$ $min^{-1}$) |
| ZO | 0.92808 | 0.09351 | 0.94314 | 0.00346 | 0.95715 | 0.00539 |
| ZFO | 0.95953 | 0.18376 | 0.98996 | 0.00963 | 0.99463 | 0.02365 |
| 5ZO@ZFO | 0.96799 | 0.294 | 0.99754 | 0.01336 | 0.09589 | 0.0475 |
| 10ZO@ZFO | 0.94077 | 0.23446 | 0.99636 | 0.01854 | 0.83975 | 0.10545 |
| 15ZO@ZFO | 0.94904 | 0.21996 | 0.9977 | 0.0184 | 0.94333 | 0.06859 |

sensitisation in the visible spectrum. The incorporation of photocatalysts gave degradation efficiencies of 14.15%, 40.19%, and 49.19% for ZO, ZFO, and 10ZO@ZFO, respectively. The enhanced performance of 10ZO@ZFO is attributed to the formation of a heterojunction between ZO and ZFO, in which ZFO acts as the primary visible-light absorber, while the UV of the light source can additionally photoexcite ZO and serve as an efficient electron-acceptor and charge-transport component. This synergistic heterostructure enhances interfacial charge transfer, inhibits electron–hole recombination, and increases reactive oxygen species production, thereby promoting phenol oxidation.[35] Because of its non-photosensitising properties,

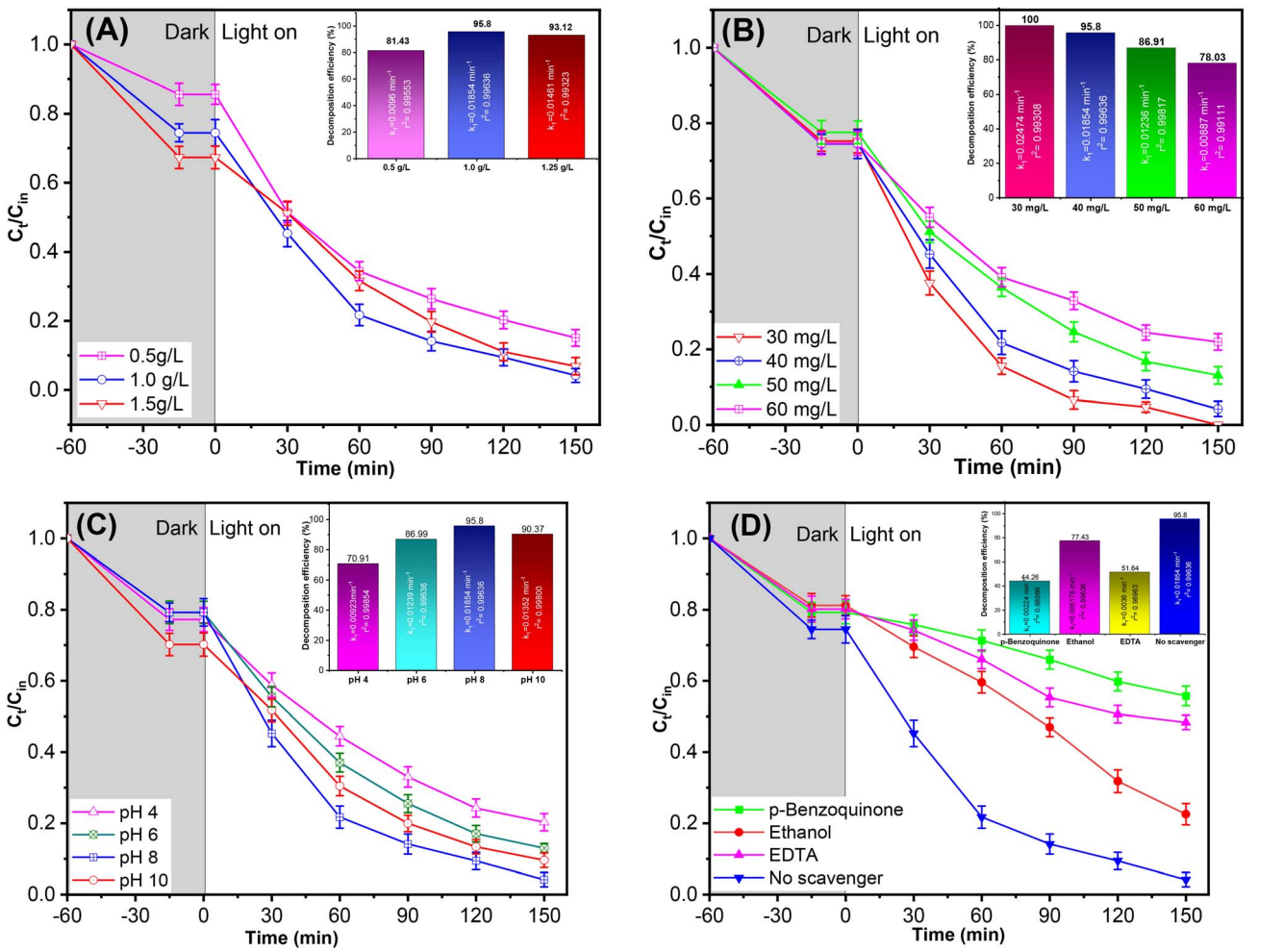


Fig. 5 (A) Effects of catalyst dosage (dosage of 10ZO@ZFO: 0.5–1.5 g $L^{-1}$; initial MB concentration: 40 ppm; pH 8). (B) Effect of initial concentration (initial MB concentration: 30–60 ppm; dosage of 10ZO@ZFO: 1.0 g L; pH 8). (C) Effect of pH (pH: 4–10; initial MB concentration: 40 ppm; dosage of 10ZO@ZFO: 1.0 g $L^{-1}$). (D) Trapping experiments (the "trapping" of free radicals $^{\bullet}OH$, $-O^{\bullet}{}_2^-$, and $h^+$ using ethanol, *p*-BQ, and EDTA).

chemical stability, and lack of visible-light absorption, phenol degrades less effectively than MB. Thus, the phenol degradation of 10ZO@ZFO depends solely on ROS generated by photocatalysis, rather than on dye sensitisation. The effective breakdown of phenol under visible light unequivocally demonstrates that 10ZO@ZFO has an authentic photocatalytic activity.

**3.2.2 Effect of catalyst loading.** Different loadings of 10ZO@ZFO affect the degradation of MB (Fig. 5A). The photocatalytic efficiency improved from 81.43% to 95.8% at loading varying between 0.75 and 1.0 mg $L^{-1}$. Nonetheless, a further increase in catalyst loading to 1.5 g $L^{-1}$ resulted in a minor reduction of photocatalytic effectiveness to 93.12%. As the catalyst loading increased, the number of active sites on the photocatalytic centre increased, leading to greater ROS production and improved degradation efficiency. However, this tendency was diminished after the addition of excessive catalyst, as excessive catalyst can create a suspension with an elevated concentration of contaminants, thereby impacting the material's light absorption capacity.[40,41]

**3.2.3 Effect of the initial concentration of MB.** Fig. 5B depicts the relationship between the initial concentration of MB and the MB breakdown efficiency of the 10ZO@ZFO. The findings demonstrate that increased MB concentration correlates with decreased MB photocatalytic decomposition efficiency. At a concentration of 30 ppm, 10ZO@ZFO destroyed MB within 150 minutes of exposure to light. The breakdown efficiencies were 95.8%, 86.91%, 85%, and 78.3% for starting MB concentrations of 40 ppm, 50 ppm, and 60 ppm, respectively. As the initial concentration of pollutants increases, more MB molecules are adsorbed onto the photocatalyst surface. The adsorption of $O_2$ and $H_2O$ on the catalyst surface decreases when an increasing number of active sites are occupied by MB molecules, thereby decreasing the generation of free radicals.[15] As the concentration of MB rises, an excess of MB molecules obstructs light transmission, resulting in incomplete activation of the catalytic centres and a reduction in MB breakdown efficiency.[26]

**3.2.4 Effect of pH.** Fig. 5C illustrates that the pH of the MB solution influenced the breakdown rate of MB of the 10ZO@ZFO. In acidic environments with pH 4 and 6, the degradation efficiency was comparatively low, achieving 70.91% and 86.99% removal of MB, respectively. The rationale was clearly elucidated by the electrostatic adsorption model, which shows that MB, a cationic dye, preferentially adsorbs to negative sites on 10ZO@ZFO. The experimental findings indicated that the zero charge point (pHpzc) of 10ZO@ZFO was 7.8. At pH 4 and 6 <pHpzc, the positively charged surface of the 10ZO@ZFO catalyst exhibited limited adsorption of cationic MB owing to electrostatic repulsion, resulting in a reduction in photocatalytic degradation. Conversely, this catalyst exhibited enhanced efficacy in an alkaline environment; at pH 8 and pH 10, the photocatalytic efficiencies for MB treatment were 95.8% ($k = 0.01854$ $min^{-1}$) and 90.37% ($k = 0.01352$ $min^{-1}$), respectively. Currently, 10ZO@ZFO has a negative charge and efficiently adsorbs MB cations, leading to improved photocatalytic degradation efficiency.[42] Experimental findings unequivocally demonstrate that the degradation efficiency of MB at pH 8 surpasses that at pH 10, as a strong alkaline environment leads to the accumulation of negatively charged $OH^-$ ions on the surface of the 10ZO@ZFO catalyst, which impedes the antagonism with MB molecules and diminishes the dye degradation rate.[40]

### 3.3 Stability and reusability

Durability and reusability are crucial factors in evaluating the photocatalytic efficacy of materials.[43] This investigation included the continuous MB photocatalytic degradation process on the 10ZO@ZFO composite sample for 150 minutes over four cycles. Following the first cycle, the 10ZO@ZFO sample was washed with distilled water, dried at 100 °C, and reused under identical photocatalytic conditions as in the first cycle. Fig. 6A displays the photocatalytic efficiency after the fourth cycle. The adsorption capacity and photocatalytic efficacy of 10ZO@ZFO decreased over the course of the cycles. The elimination efficiencies of MB after four cycles were 95.8%, 92.1%, 87.7%, and 81.5%, respectively. The XRD patterns (Fig. 6B) show the characteristic diffraction peaks of the

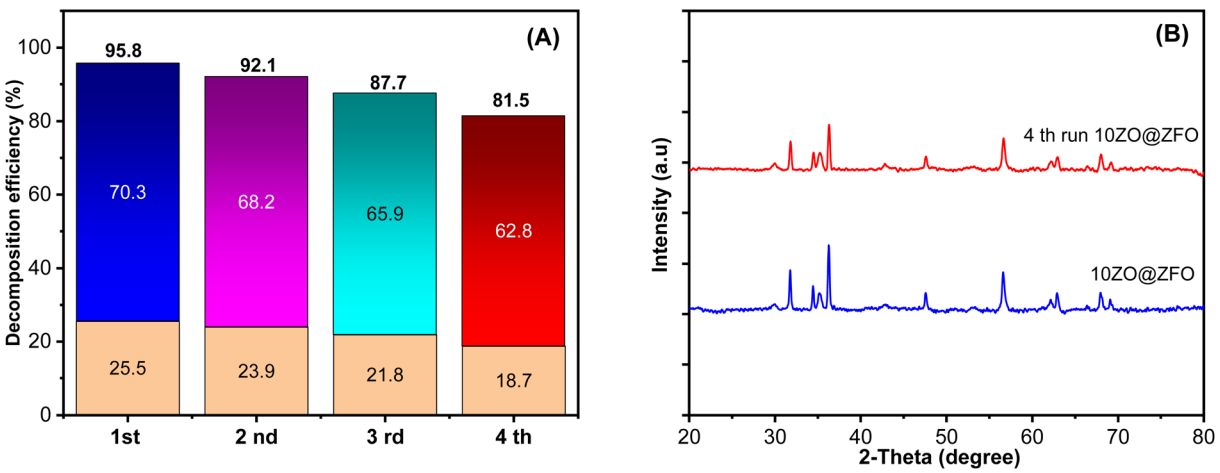


Fig. 6 (A) Cycle experiments of MB degradation of 10ZO@ZFO and (B) XRD patterns of 10ZO@ZFO before and after the 4th cycle.

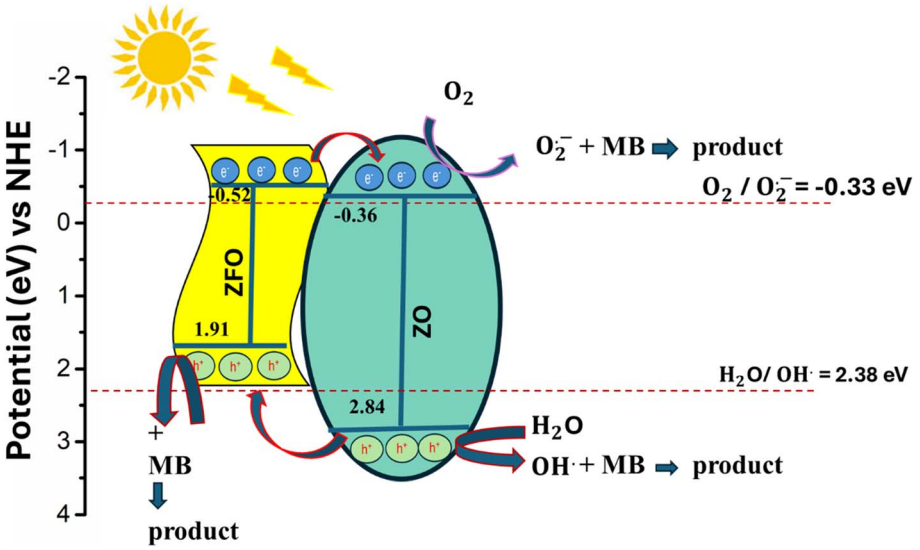


Fig. 7 Mechanism of degradation of MB by ZO@ZFO.

10ZO@ZFO sample and the sample after the 4th cycle. The primary diffraction peaks associated with the 10ZO@ZFO phase remain discernible, with no significant widening or shifting, indicating that the composite material's crystal structure is preserved after four cycles. The results indicate that 10ZO@ZFO is both reusable and very stable.[28] Nevertheless, the diffraction peaks for 10ZO@ZFO in the fourth cycle were weaker than in the initial state, likely due to the accumulation of by-products on the material's surface during the four successive cycles.

### 3.4 Photodegradation mechanism

To determine the primary active species produced by the 10ZO@ZFO material during the MB degradation process, an active radical trapping was introduced into the reaction system.[44] The trapping experiment was conducted using the same photocatalytic process shown in Fig. 5D. Experimental results indicated that the degradation efficiency of MB in the reaction system with the addition of *p*-BQ (1.0 mM) and EDTA (0.5 mM) significantly declined to 44.26% and 51.64%, respectively, compared with 95.8% in the absence of trapping. Conversely, upon the introduction of ethanol (0.5 mM), the efficiency of MB removal decreased significantly. Consequently, the trapping experiment indicated that in the photocatalytic degradation of MB, $h^+$ and $O^{\bullet}{}_2^-$ were the primary contributors, whereas $^{\bullet}OH$ provided assistance. The efficacy of ROS in the degradation of MB was ranked as follows: $O^{\bullet}{}_2^- > h^+ > {}^{\bullet}OH$.

Based on the trap and reduction potential test results for the VB and CB of ZO and ZFO, determined in Section 3.1, it is expected that the photocatalytic degradation of MB by ZO@ZFO will follow a type II mechanism (Fig. 7). In the presence of light, the electrons in the VB of the semiconductors ZO and ZFO absorb photons and transition to their CB, resulting in the formation of photogenerated electron–hole pairs ($e^-/h^+$).[26] In CB, the reduction potentials of ZO and ZFO are more negative than the reduction potential of $O_2/O^{\bullet}{}_2^-$ ($E = -0.33$ eV), enabling these electrons to combine with $O_2$ adsorbed on the material surface to create $O^{\bullet}{}_2^-$ for the decomposition of MB. However, because the reduction potential of ZFO ($E_{CB} = -0.52$ eV) is more negative than that of ZO ($E_{CB} = -0.36$ eV), the electrons of ZFO also move to ZO to carry out the $O_2$ reduction process, forming $O^{\bullet}{}_2^-$ to decompose the MB.[30,36] In VB, the reduction potential of ZO ($E_{VB} = 2.84$ eV) is higher than the reduction potential of ZFO ($E_{VB} = 1.91$ eV) and the standard reduction potential of $H_2O/{}^{\bullet}OH$ ($E_{H_2O/{}^{\bullet}OH} = 2.4$ eV), so the $h^+$ in ZO moves to ZFO, combines with the $h^+$ of ZFO to directly decompose MB, or potentially oxidize H2O to create $^{\bullet}OH$ so as to decompose MB.[17,30] However, the photogenerated holes in ZFO cannot oxidise $H_2O$ to create $^{\bullet}OH$, so the reduction potential is smaller than the standard reduction potential of $H_2O/{}^{\bullet}OH$. The heterojunction between ZO and ZFO enhances the production of active oxygen species in these photocatalytic materials by facilitating photogenerated electron transfer across the demonstrated heterojunction and preventing recombination with holes *via* inherent electric-field effects.

## 4. Conclusions

Co-precipitation was used to successfully prepare Zn/Fe-LDHs, which were then calcined to form MMOs and dispersed at different mass ratios on ZnO nanosheet rods. A photocatalytic study revealed that the ZO@ZFO sample exhibited exceptional performance at a ZO/ZFO mass ratio of 10%, resulting in nearly complete MB breakdown (95.8%, $k_1 = 0.01854\ min^{-1}$) after 150 minutes of illumination. The results indicated a chemical interaction between ZO and ZFO, which modified the composite's light absorption. The ZO@ZFO composite's large surface area and strong photon absorption capabilities improved its photocatalytic effectiveness, ascribed to the synergistic effects that significantly reduced recombination. The photocatalytic degradation mechanism of MB by ZO@ZFO is elucidated as a conventional type II heterojunction, with $h^+$ and $O^{\bullet}{}_2^-$ identified as the primary contributors to the catalytic process. The photocatalytic degradation efficiency of ZO@ZFO reached

81.5% after 4 cycles, demonstrating its considerable potential for treating polluted water.

## Author contributions

Nguyen Thi Mai Tho participated in methodology, validation, and project administration. Huynh Tu Khanh conducted a study of photocatalyst activity. Minh An Tran Nguyen contributed to the writing, reviewing, and editing of the draft manuscript. T. V. M. Sreekanth and Nguyen Thi Hong Anh participated in the editing of the draft manuscript.

## Conflicts of interest

The authors declare that they have no known competing interests that could affect the research described in this publication.

## Data availability

Data availability statement is available at https://doi.org/10.6084/m9.figshare.30817034.

## Acknowledgements

This work is supported by the Industrial University of Ho Chi Minh City (IUH), Ho Chi Minh, Vietnam.

## References

1 T. Jamil, *Desalin. Water Treat.*, 2024, **318**, 100387.
2 D. M. Osorio-Aguilar, H. A. Saldarriaga-Noreña, M. A. Murillo-Tovar, J. Vergara-Sánchez, J. Ramírez-Aparicio, L. Magallón-Cacho and M. L. García-Betancourt, *Catalysts*, 2023, **13**(12), 1480.
3 D. Pan, S. Ge, J. Zhao, Q. Shao, L. Guo, X. Zhang, J. Lin, G. Xu and Z. Guo, *Dalton Trans.*, 2018, **47**, 9765–9778.
4 M. Cheng, G. Zeng, D. Huang, C. Lai, P. Xu, C. Zhang and Y. Liu, *Chem. Eng. J.*, 2016, **284**, 582–598.
5 B. Weng, M. Zhang, Y. Lin, J. Yang, J. Lv, N. Han, J. Xie, H. Jia, B.-L. Su, M. Roeffaers, J. Hofkens, Y. Zhu, S. Wang, W. Choi and Y.-M. Zheng, *Nat. Rev. Clean Technol.*, 2025, **1**, 201–215.
6 J. Shen, A. Shi, J. Lu, X. Lu, H. Zhang and Z. Jiang, *Environ. Pollut.*, 2023, **323**, 121186.
7 Y. Ai, S. A. C. Carabineiro, X. Xiong, H. Zhu, Q. Wang, B. Weng and M. Q. Yang, *Chin. J. Catal.*, 2025, **75**, 147–163.
8 S. Soni, A. Kumari, A. Sharma, A. Sharma, V. Sheel, S. K. Bhatia and A. K. Sharma, *J. Indian Chem. Soc.*, 2025, **102**, 102198.
9 J. Guo, C. Luo, P. Li, M. Ye, Z. Qiao, Y. Wu, H. Hu, X. Luo, L. Yang, Y. Cai, P. Li, K. Zhu, C. Fu, B. Yu, Y. Chen, S. Wang, T. Wang, C. Qi, Z. Liu, D. Huang, Z. Wei, F. Mao, Y. Wei, C. Wen, C. Han, B. Weng, H. Feng, J. Hong, J. Wu, Y. Xiao, G. Liu, L. Song, R. Ren, Z. Wang, L. Kong, H. Shang, L. Wang, Y. Chen, C. Ou, H. Yang, X. Liu, J. Yi, S. Li, C. Yu, Y. Cao, Z. Wu, Y. Deng, W. Hu, J. Zhong, X. Zhang, Y. Ma and J. Ma, *Chin. Chem. Lett.*, 2026, **37**, 112116.
10 D. Peng and Y. Zhang, *Appl. Catal., A*, 2023, **653**, 119067.
11 A. F. Denti, J. L. Bernardi, B. M. S. Puton, G. M. Bruel, A. Junges, J. Steffens and R. M. Dallago, *J. Photochem. Photobiol., A*, 2025, **459**, 116068.
12 Y. Zhu, P. Wu, S. Yang, Y. Lu, W. Li, N. Zhu, Z. Dang and Z. Huang, *RSC Adv.*, 2016, **6**, 37689–37700.
13 S. Bin Lee, E. H. Ko, J. Y. Park and J. M. Oh, *Nanomaterials*, 2021, **11**, 1153.
14 F. J. A. G. Coumans, S. Mitchell, J. Schütz, J. Medlock and J. Pérez-Ramírez, *ACS Omega*, 2018, **3**, 15293–15301.
15 F. Z. Janani, H. Khiar, N. Taoufik, M. Sadiq, L. Favier, A. O. Ezzat, A. Elhalil and N. Barka, *Environ. Sci. Pollut. Res.*, 2024, **31**, 25373–25387.
16 T. Zheng, H. Wu, Z. Han, L. Chen, B. Tang, P. Cui, H. Liu, Y. Chao, W. Zhu and Z. Liu, Boron nitride modified CuZn-calcinated layered double hydroxides as efficient adsorbents for tetracycline removal, *Sep. Purif. Technol.*, 2024, **340**, 126648.
17 L. Liu, G. Zhao, S. Zhou, Y. Wang and F. Jiao, *J. Mater. Sci.: Mater. Electron.*, 2021, **32**, 11489–11502.
18 N. H. Nam, N. Q. Hung, N. T. H. Anh, N. Q. Thang and N. T. M. Tho, *RSC Adv.*, 2024, **14**, 32436–32450.
19 J. S. Prabagar, D. Vinod, Y. Sneha, K. M. Anilkumar, S. Rtimi, K. Wantala and H. P. Shivaraju, *Environ. Sci. Pollut. Res.*, 2023, **30**, 90383–90396.
20 Y. Zhang, J. Zhou, Z. Li and Q. Feng, *J. Mater. Sci.*, 2018, **53**, 3149–3162.
21 P. K. Aspoukeh, A. A. Barzinjy and S. M. Hamad, Synthesis, properties and uses of ZnO nanorods: a mini review, *Int. Nano Lett.*, 2022, **12**, 153–168.
22 S. V. Gudkov, D. E. Burmistrov, D. A. Serov, M. B. Rebezov, A. A. Semenova and A. B. Lisitsyn, *Front. Phys. A*, 2021, **9**, 641481.
23 P. K. Samanta and A. K. Bandyopadhyay, *Appl. Nanosci.*, 2012, **2**, 111–117.
24 T. V. M. Sreekanth, H. P. Dang, N. Q. Thang, N. Van Cuong and N. T. M. Tho, Synthesis of calcined LDHs materials decorated on ZnO nanorods: enhancing adsorption capacity and antibacterial activity, *Environ. Sci.:Adv.*, 2025, **4**, 663–675.
25 H. Chen, W. Liu and Z. Qin, *Catal. Sci. Technol.*, 2017, **7**, 2236–2244.
26 D. Varghese, M. Joe Raja Ruban, P. Joselene Suzan Jennifer, D. AnnieCanisius, K. Ramya, S. Muthupandi, J. Madhavan and M. Victor Antony Raj, Visible light-driven photocatalytic removal of tetracycline healthcare waste by retrievable $ZnFe_2O_4$/MWCNTs nanocomposite, *J. Mater. Sci.: Mater. Electron.*, 2024, **35**, 279.
27 M. Zouhier, K. Tanji, J. A. Navio, M. C. Hidalgo, C. Jaramillo-Páez and A. Kherbeche, Preparation of $ZnFe_2O_4$/ZnO composite: Effect of operational parameters for photocatalytic degradation of dyes under UV and visible illumination, *J. Photochem. Photobiol., A*, 2020, **390**, 112305.
28 F. S. Khliwi and H. A. Alshamsi, Design of a Z-Scheme System with g-$C_3N_4$/$WO_3$/$ZnFe_2O_4$ Nanocomposite for Photocatalytic Degradation of Rhodamine B, *J. Cluster Sci.*, 2025, **36**, 99.

29 N. Akter, T. Ahmed, I. Haque, M. K. Hossain, G. Ray, M. M. Hossain, M. S. Islam, M. A. Ali shaikh and U. S. Akhtar, XPS valence band observable light-responsive system for photocatalytic acid Red114 dye decomposition using a ZnO–$Cu_2O$ heterojunction, *Heliyon*, 2024, **10**, 30802.
30 M. Shao, A. Wang, H. Cui, Z. Liu, Y. Xu, Z. Li and S. Xu, *J. Mater. Sci.: Mater. Electron.*, 2020, **31**, 1472–1482.
31 A. S. Eltaweil, K. Samir, E. M. Abd El-Monaem and G. M. El-Subruiti, *RSC Adv.*, 2025, **15**, 33549–33560.
32 Q. Wang, X. Zong, L. Tian, Y. Han, Y. Ding, C. Xu, R. Tao and X. Fan, $Fe_2O_3$/$FePO_4$/FeOOH Ternary Stepped Energy Band Heterojunction Photoanode with Cascade-Driven Charge Transfer and Enhanced Photoelectrochemical Performance, *ChemSusChem*, 2022, **15**, e202102377.
33 B. Pan, S. Wang, G. Li and L. Zou, *Mikrochim. Acta*, 2025, **192**, 730.
34 K. Wang, Q. Chen, H. Xie, M. Wang, X. Kong, K. Cheng and Z. Jin, *Catal. Lett.*, 2024, **154**, 6227–6240.
35 L. Zou, H. Wang, G. Yuan and X. Wang, *ACS Appl. Nano Mater.*, 2018, **1**, 831–838.
36 L. Li, W. Jianhua and H. Fang, Fabrication of $ZnFe_2O_4$@g-$C_3N_4$ for Enhanced Photo-Fenton Effect and Visible Light-Driven Organic Dye Degradation, *Sci. Rep.*, 2025, 21707.
37 M. Bagheri, M. Y. Masoomi, A. Forneli and H. García, *J. Phys. Chem. C*, 2022, **126**, 683–692.
38 N. Alomayrah, M. Ikram, S. Zulfiqar, S. Alomairy, M. S. Al-Buriahi, I. Shakir, M. F. Warsi and E. W. Cochran, *RSC Adv.*, 2024, **14**, 24874–24897.
39 M. S. AlSalhi, S. Devanesan, N. Asemi and A. Ahamed, Concurrent fabrication of ZnO–$ZnFe_2O_4$ hybrid nanocomposite for enhancing photocatalytic degradation of organic pollutants and its bacterial inactivation, *Chemosphere*, 2023, **18**, 137928.
40 N. D. Dien, T. T. H. Pham, X. H. Vu, V. T. Xuan, T. T. T. Nguyen, T. T. Trang, N. Van Hao, P. T. Nga, T. T. Kim Chi, T. T. H. Giang and N. D. Toan, *RSC Adv.*, 2024, **14**, 28244–28259.
41 S. Luo, Z. Pang, N. Ding and H. Liu, *Res. Chem. Intermed.*, 2023, **49**, 5517–5539.
42 M. T. Uddin, M. Z. Bin Mukhlish and M. R. H. Patwary, *Desalin. Water Treat.*, 2021, **212**, 311–322.
43 R. Saleem, H. Shaikh, M. S. Barhaam, G. M. Thebo, M. A. Abbasi, N. M. Shaikh, M. A. Bhatti, E. Dawi, A. Tahira, A. Nafady, S. Ata, M. Tonezzer, Z. H. Ibupoto and J. Facile, Facile synthesis of ZnO@NiFe-LDH nanocomposites for efficient photocatalytic degradation of methylene blue under natural sunlight irradiation, *Sci. Technol.*, 2025, **116**, 179–192.
44 M. Y. Masoomi, M. Bagheri and A. Morsali, *CrystEngComm*, 2017, **19**, 5749–5754.